UNSTEADY AERODYNAMIC EFFECTS OF TRAILING EDGE CONTROLS ON DELTA WINGS

D.J. Pilkington* and N.J. Wood**
School of Mechanical Engineering,
University of Bath,
Bath, UK.

ABSTRACT

Effective control of combat aircraft at high angles-of-attack requires the Flight Control System to operate to higher frequencies and gains. This increases the possibility of excitation of the structural modes. This paper details the results of tests carried out on a rigid, 55° leading edge sweep delta wing, half model fitted with a half span elevon operated through a closed loop control system. The effects of steady elevon deflections up to 40° angle-of-attack are described. The unsteady pressures resulting from elevon oscillations at frequency parameters up to a value equivalent to the first wing bending mode of a typical combat aircraft have been measured. The effect of the elevon oscillation on the elevon itself and on the bending mode have been estimated by calculating the unsteady hinge and root bending moments about the wing root. The lower surface, unsteady elevon effects were found to be independent of incidence and frequency parameter. The amplitude of response of the weak vortex on the upper surface of the wing reduced rapidly with frequency parameter. Above an incidence of 10°, the vortex breakdown was above the wing and led to a further reduction in the vortex response. The vortex response lagged the elevon motion.

NOMENCLATURE

A	- inertia matrix	
B	- aerodynamic damping matrix	
C	- aerodynamic stiffness matrix	
C_n	- normal force coefficient	
C_p	- pressure coefficient ($p/\frac{1}{2}\rho V^2$)	
c_η	- elevon chord	(m)
D	- structural damping matrix	
E	- structural stiffness matrix	
h	- hinge moment coefficient	
i	- complex identifier $\sqrt{(-1)}$	
K	- pressure amplitude ratio	
p	- pressure	(N/m^2)
q	- degrees of freedom column matrix	
r	- wing root bending moment coefficient	
s	- wing semi-span	(m)
S	- wing area of model	(m^2)
S_η	- elevon surface area	(m^2)
t	- time	(s)
u	- control deflection matrix	
V	- freestream velocity	(m/s)
x	- distance from apex along centreline	(m)
X	- state equation matrix	
y	- spanwise distance from root	(m)
Y	- control influence matrix	
α	- angle-of-attack	(degrees)
η	- elevon angle	(rads)
ν	- frequency parameter ($\omega s/V$)	
ρ	- air density	(kg/m^3)
ϕ	- phase angle	(rads)
ω	- angular velocity	(rads/s)

Subscripts

h	- hinge moment
m	- mean
o	- amplitude
r	- root bending moment
trans	- pressure transducer
wing	- wing tapping reading
ω	- component at this frequency
η	- resulting from elevon oscillation

Superscripts

'	- in phase component
"	- out of phase component

* Postgraduate Researcher
** Senior Lecturer

INTRODUCTION

Attempts to increase the manoeuvrability of combat aircraft have involved the investigation of high-angle-of-attack flight for delta wing configurations. For effective control and manoeuvrability in this part of the flight envelope, the nature of the unsteady aerodynamics produced by the complex, attached flow and vortex dominated separated flow must be understood. Knowledge of the level of interaction with the aircraft structural modes and control system dynamics is also essential. Various researchers (Ross[1], Orlik-Rückemann[2], Lang et. al.[3] and Williams et. al.[4]) have suggested the Flight Control System (FCS) would need to operate to higher frequencies and gains in order to provide a stable platform under these extreme conditions, thus increasing the potential for structural interactions.

Consider the classical flutter equation for a flexible structure,

$$A\ddot{q} + (D + \rho VB)\dot{q} + (E + \rho V^2 C)q = 0$$

Each matrix A, B, C, D, E, is formed from the various rigid and flexible modes of the aircraft, as given in fig. 1. The column matrix, q, represents the degrees of freedom and each generalised mode displacement. The equation could also be written in state equation form, as commonly used in FCS analysis, i.e.

$$\dot{q} = Xq + Yu$$

Here q would represent both displacements and first derivatives as separate elements, and u the control deflections.

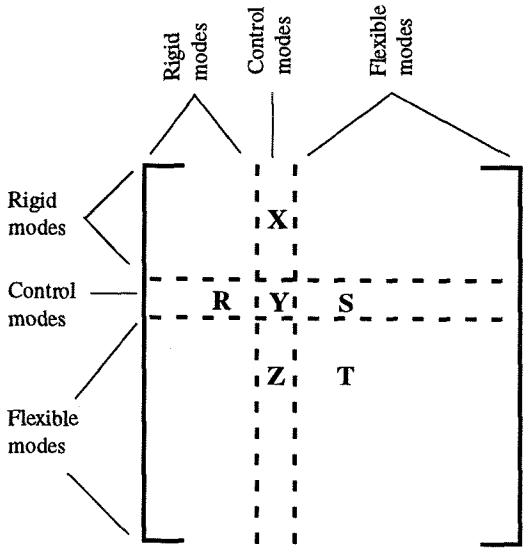

Fig. 1 - *flutter equation matrix.*

In fig. 1, X is the effect of the control modes (typically rotation about its hinge axis) on the aircraft rigid modes (e.g. pitch effect), whilst Y is the direct control effect on itself and Z is the effect on the flexible modes, the main one of interest for the present work being the first wing bending mode. Elements R and S are the effects of the rigid and flexible modes on the control and T is the effect of the wing bending mode on itself.

The research programme, of which the work reported here is a part, was designed to produce an understanding of the unsteady aerodynamic interactions occurring between the control surface and main wing aerodynamics and to determine values for R, S, T and X, Y, Z in fig. 1, at high angles-of-attack for a typical combat aircraft wing geometry.

The work presented in this paper was designed to obtain the steady and unsteady pressures resulting from steady trailing edge elevon deflections and from elevon oscillations (up to frequencies equivalent to a typical first wing bending mode for delta wing, combat aircraft across a wide range of incidences). These results give an indication of the characteristic responses of the flow types experienced on these wing geometries. The actual influence of the elevon on the various modes can be calculated by multiplying the unsteady pressures from the rigid model tests by the relevant mode shape, thus giving the matrix terms X, Y, Z in fig. 1.

Other components of the programme will determine the unsteady pressures associated with the bending mode itself, and the effect on the elevon, to determine elements S and T from fig. 1. The level of structural excitations predicted from the solution of the flutter equation for elevon rotation and wing bending modes, i.e. just elements S, T and Y, Z, will be compared with the response to elevon oscillations of a model with both degrees of freedom present. This will evaluate the accuracy of the classical flutter equation at high angles-of-attack where the flow is naturally very unsteady and large scale interactions can occur.

This research is supported by the Science and Engineering Research Council and British Aerospace Defence Ltd., Military Aircraft Division, Warton, UK.

EXPERIMENTAL DETAILS

Pressure Tapped Half Model

A 55° leading edge sweep, rigid half wing was constructed with 157 unsteady pressure tappings in the upper surface (fig. 2). The model had a 0.3m semi-span, root chord of 0.528m, with a leading edge bevel on the lower surface of 22° normal to the leading edge. Each tapping was formed by laying a stainless steel tube in the surface of the wing, the tapping being formed by drilling

perpendicularly into the end. Each tube was connected to a port on a multi-barrel Scanivalve® unit via a 1m length of VYL-040® Scanivalve tubing.

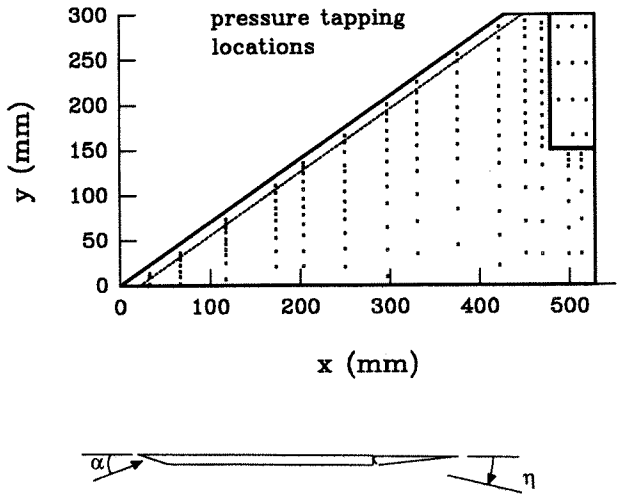

Fig. 2 - *pressure tapping locations and section of model.*

Using this form of tubing system introduced a dynamic calibration effect between the pressure at the surface of the wing, p_{wing}, and the statically calibrated pressure signal at the transducer within the Scanivalve®, p_{trans}, i.e.

if $$p_{wing} = p_o \sin(\omega t)$$

then,

$$p_{trans} = K.p_o \sin(\omega t + \phi)$$

where K is the amplitude ratio and ϕ is the phase angle.

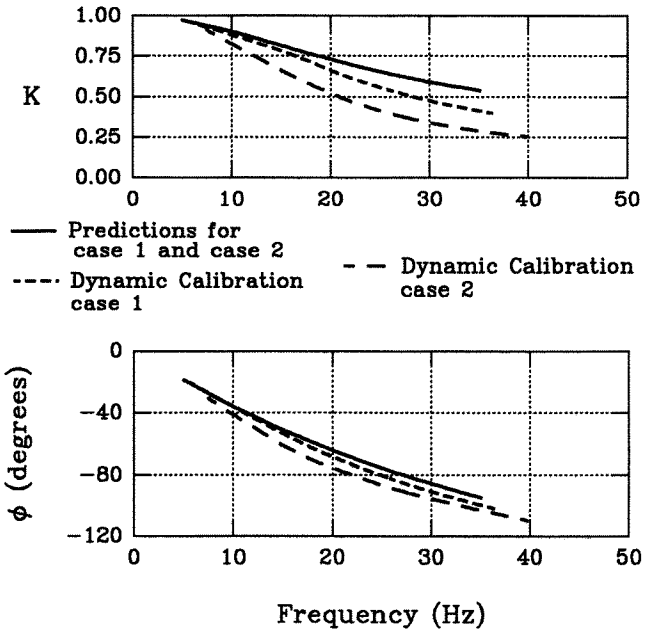

Fig. 3 - *typical tubing dynamic calibrations.*

The theoretical predictions of Bergh and Tijdeman[5,6] were originally used to determine this dynamic calibration, however, they did not predict the effect with sufficient accuracy. Indeed, supposedly identical tubes in the model were found to have different measured dynamic calibrations, as shown in fig. 3. It was thus necessary to calibrate each tube system individually using test apparatus capable of producing oscillatory pressures. Using this technique, the effect of the local static pressure and local flow velocity over the tapping could not be allowed for. By performing wind-on check calibrations, these effects were found to be within the repeatability of the results. The estimated accuracy of the dynamic calibrations are ±3% in phase and ±5% in amplitude.

The model was fitted with two equal size trailing edge control surfaces. The inboard elevon was held fixed at 0°. The outboard control was constructed using a foam core with carbon fibre skin, thus producing a stiff, low inertia elevon. The control was actuated by a Pitman® brushless d.c. motor and controller, through a closed loop control system, giving an angle demanded by a PC (see fig. 4). The control angle, η, was measured at the root of the elevon using a Hall effect sensor, rather than from the encoder used for feedback in the control system.

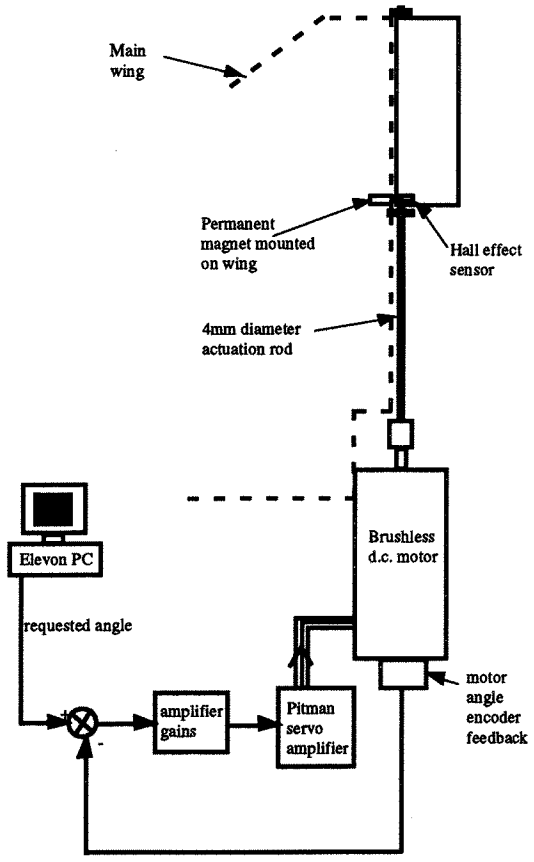

Fig. 4 - *elevon actuation system.*

Wind Tunnel Mounting Arrangement

The model was tested in the University of Bath, 2.13m × 1.52m, Low Speed Wind Tunnel. Due to the tunnel boundary layer, the model was supported away from the ceiling of the tunnel using a circular splitter plate (fig. 5). By mounting the model to a rotating balance plate above the tunnel, it was possible to adjust the angle-of-attack, α, to ±90°. The lowest natural frequency of the model when supported from the balance was 65Hz. No significant structural excitation of the rigid wing was measured during the tests.

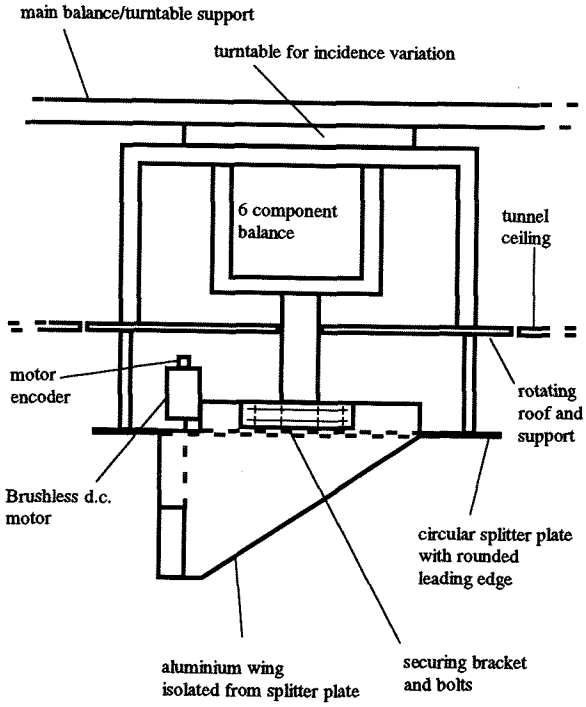

Fig. 5 - *half model mounting arrangement.*

Test Parameters

All the results presented were for a tunnel speed of 30m/s, giving a Reynolds Number of 2.02×10^6 per metre. Tests were performed for $\alpha=\pm40°$, negative angles giving the lower surface pressures. The pressures for steady elevon deflection angles of $\eta=0°$ and ±10° were measured.

The unsteady aerodynamics resulting from elevon oscillations at various frequencies were measured. These tests can be related to the actual aircraft by matching the frequency parameter values, $\nu=\omega s/V$. Since the flexible mode of interest was the wing first bending mode (usually the lowest frequency, wing structural mode, giving $\nu=1.5$ for a typical combat aircraft) it was necessary to oscillate the elevon through a range of $\nu=0.32$ - 1.65. This equates to a maximum elevon oscillation frequency of 25 Hz at model scale. All oscillations were about a mean of $\eta=0°$, with amplitude of 5°.

ANALYSIS OF UNSTEADY PRESSURES

Assuming a sinusoidal oscillation of the elevon, $\eta(t)$, where,

$$\eta(t) = \eta_o \sin(\omega t) + \eta_m$$

and considering only the pressure component at this frequency, $C_{p_\omega}(t)$, then

$$C_{p_\omega}(t) = C_{p_o} \sin(\omega t + \phi) + C_{p_m}$$

A complex Fast Fourier Analysis of both the elevon angle and the unsteady pressure produces results of the form

$$C_p(\nu) = C_p'(\nu) + iC_p''(\nu)$$

$$\eta(\nu) = \eta'(\nu) + i\eta''(\nu)$$

A transfer function between the unsteady pressure component and the elevon at frequency parameter, ν, can be formed, i.e.

$$\frac{C_p}{\eta}(\nu) = C_{p_\eta}(\nu) + iC_{p_{\dot\eta}}(\nu)$$

$$\text{where} \quad \nu = \frac{\omega s}{V}$$

or in polar form:

$$\frac{C_p}{\eta}(\nu) = \frac{C_{p_o}}{\eta_o}\sin(\phi)$$

$$\text{where} \quad \frac{C_{p_o}}{\eta_o} = \sqrt{C_{p_\eta}^{\,2} + C_{p_{\dot\eta}}^{\,2}}$$

$$\phi = \tan^{-1}\frac{C_{p_{\dot\eta}}}{C_{p_\eta}}$$

Hence, the pressure amplitude is non-dimensionalised with elevon oscillation amplitude, (C_{po}/η_o), with a phase angle, ϕ, between pressure and elevon.

A program was written to produce the required analysis. It applies the dynamic tube calibrations and performs a Fourier Analysis on both the elevon angle and the unsteady pressure coefficient. By dividing the complex FFTs, the transfer function is obtained. A flowchart of the program is given in fig. 6.

Rather than present values for the elements in the matrix of fig. 1, this paper shows values for the unsteady, aerodynamic hinge moments acting on the elevon and for the unsteady aerodynamic, rigid wing, bending moment about the wing root calculated by integrating the surface pressures as defined below:

Integrating over the elevon,

$$h_\eta(v) = \frac{1}{2S_\eta c_\eta}\int_0^{S_\eta} C_{p_\eta}(x - x_h)\, dA_\eta + i\frac{1}{2S_\eta c_\eta}\int_0^{S_\eta} C_{p_{\dot\eta}}(x - x_h)\, dA_\eta$$

or in polar form,

$$h_\eta(v) = h_o \sin(\phi_h)$$

and over the whole wing and elevon,

$$r_\eta(v) = \frac{1}{2Sc}\int_0^{S} C_{p_\eta}.y\, dA + i\frac{1}{2Sc}\int_0^{S} C_{p_{\dot\eta}}.y\, dA$$

or in polar form,

$$r_\eta(v) = r_o \sin(\phi_r)$$

All the unsteady results will be presented in polar form.

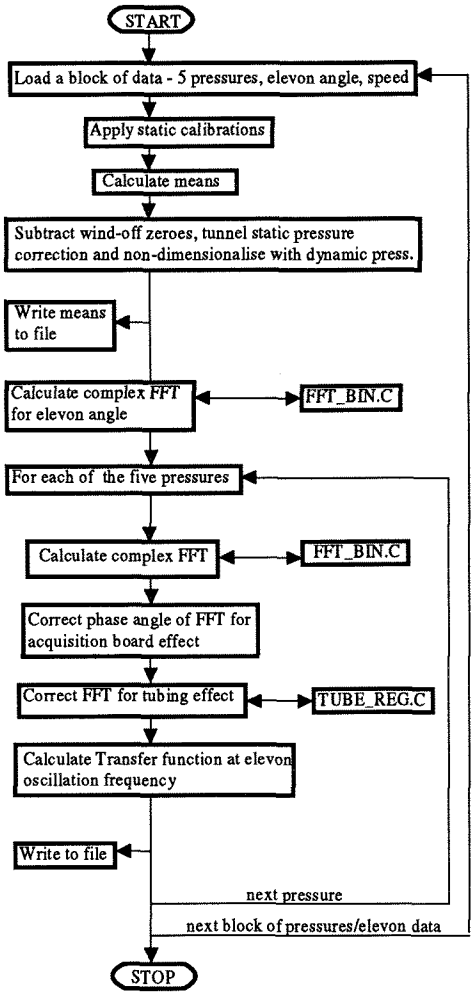

Fig. 6 - *flowchart of data analysis program.*

The use of a half model implies symmetry of elevon motion and aerodynamic response about the wing root, and hence the mode considered is symmetric elevon deflection with resulting symmetric vortex response. It is known, however, that significant asymmetry of steady vortex breakdown location can occur at high angles-of-attack. The use of a half model can not allow for this effect.

STEADY PRESSURE RESULTS

Before considering the unsteady pressures it is important to establish the steady flow phenomenon and the effects of fixed elevon deflections.

The upper surface pressures at α=10°, 12.5°, 15°, 20°, 27.5° and 35° are presented in fig. 7.

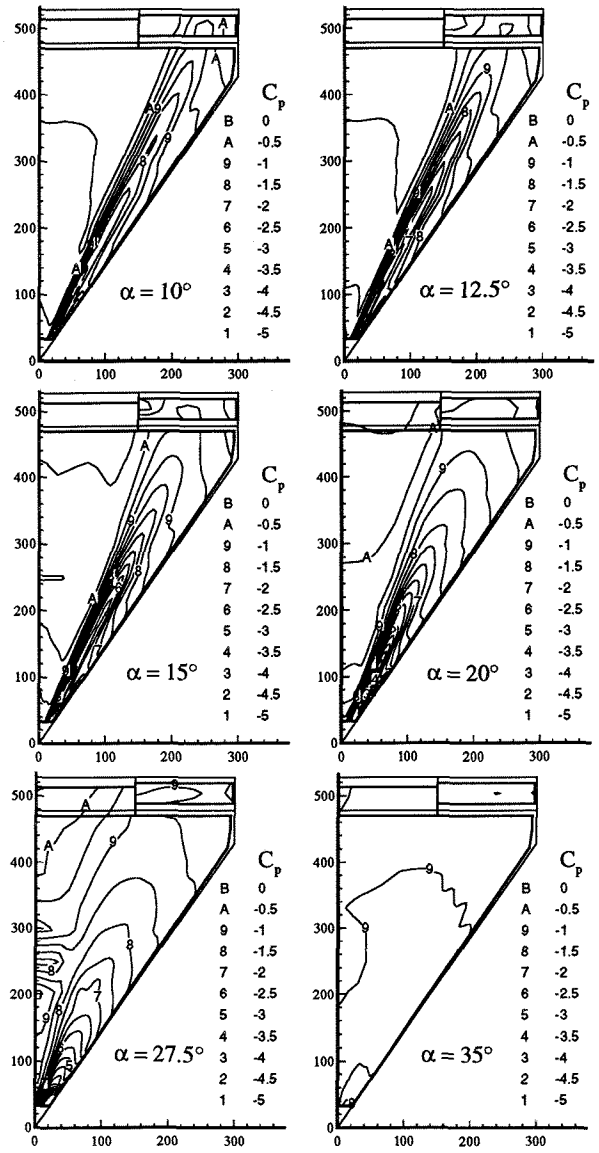

Fig. 7 - *upper surface, steady pressures.*

The location of the vortex suction on the wing can be seen from the strength of the pressure levels in fig. 7. As α increases, so the suction and hence vortex strength increases. Above α=12.5°, the vortex suction towards the trailing edge begins to diffuse in the y direction and decrease in strength, suggesting the vortex burst is over the wing. The burst point continues to move towards the apex as α increases. Eventually the vortex is no longer evident on the wing and the pressures resemble those present on the leeward side of a bluff body (α=35°)

By integrating the steady pressure results at fixed angles-of-attack and elevon angle, η=0°, the normal force coefficient, C_N, given on fig. 8 was obtained. The wing stalls at α=28°, when the vortex burst is at the apex of the wing.

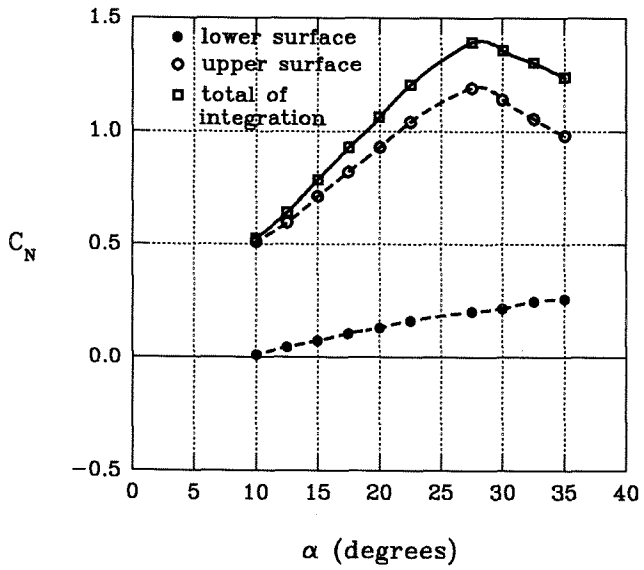

Fig. 8 - *normal force curve.*

Fig. 9 shows the variation with x of C_{pmin} at these α. From these results and surface flow visualisation, the following characteristics of the flow were determined. The vortex breakdown location appears on the wing between α=10°-12.5°. The relative weakness of the vortex (compared to more highly swept wings), as shown by the C_{pmin} values, makes it difficult to accurately locate the position of the burst. Slender body theory predicts that, for an unburst vortex, the suction under the vortex should increase at each location with α. At α=12.5°, the C_{pmin} values in fig. 9 display a 'kink' at x=400mm, and suggests this as the location of the burst point on the wing surface. In front of this point the value becomes more negative, whilst towards the trailing edge, i.e. under the burst portion of the vortex, the value increases to the value present at α=10°. The surface contours also begin to diffuse in the y-direction at this value of x (fig. 7). A similar analysis at α=15° suggests the burst point is at x=260mm. The variations in C_{pmin} closer to the apex is due to a lack of pressure tappings in this region.

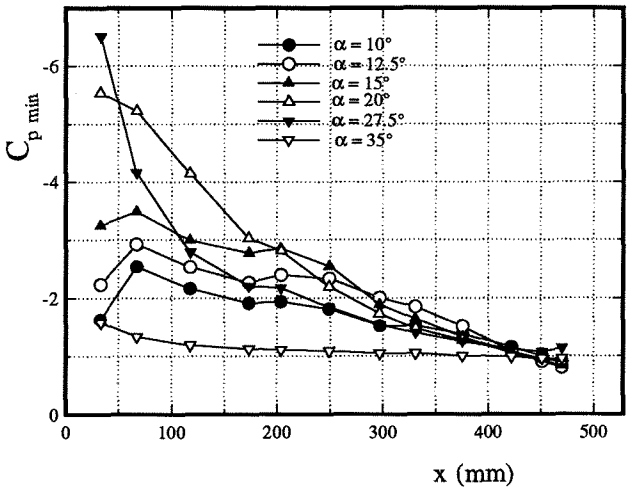

Fig. 9 - *peak vortex suction variations.*

Fig. 10 shows in more detail the vortex burst effect on the pressure distributions, by considering the row of tappings at x=375.5mm. For α=12.5°, the suction peak under the primary vortex is stronger than at α=10° and is slightly inboard of it. At α=15°, the vortex burst is in front of this station, resulting in a much lower suction level and a broader peak. Above α=20°, it is difficult to locate the burst point, but it appears to continue to move closer to the apex.

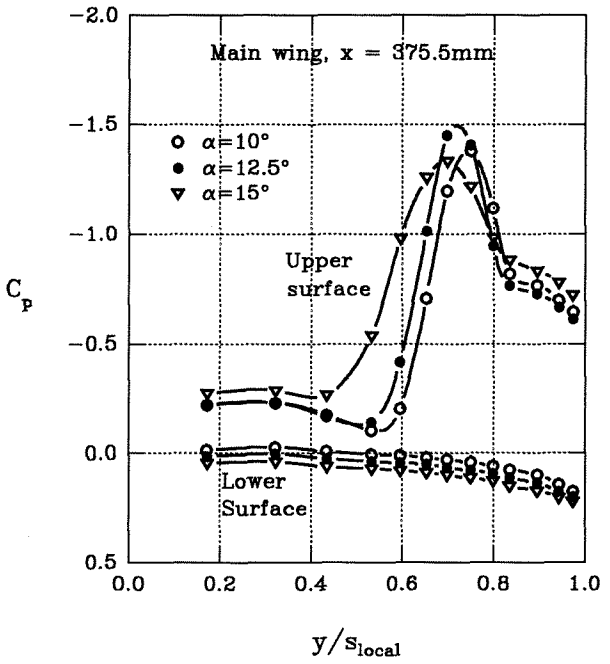

Fig. 10 - *pressure distributions for burst and unburst vortex.*

The lower surface pressure contours at α=10°, 15° and 20° are given in fig. 11. These are as expected for fully attached flow, although the vortex on the upper surface appears to have an effect on the pressure distribution over the lower surface of the elevon.

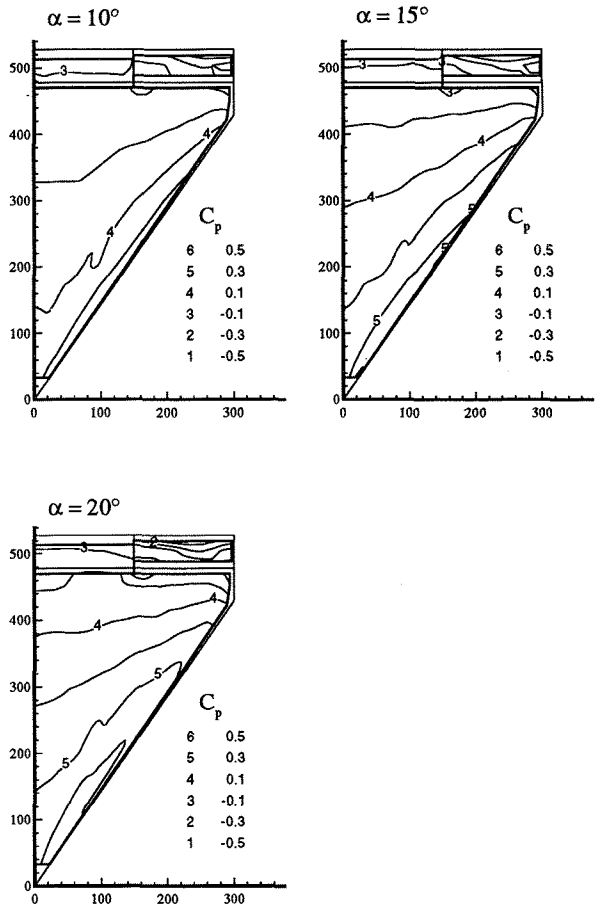

Fig. 11 - *lower surface pressure contours.*

The effect of elevon deflection on the surface pressures can be seen from fig. 12(a) to (e). These show the incremental pressures, $\Delta C_p/\Delta\eta$, for a mean elevon angle, η=0°. Consider first the upper surface. At α=10°, a positive deflection causes increased suction under the vortex (ΔC_p is negative under the suction peak associated with the vortex). These change could be associated with either a change in the vertical position of the core of the vortex or from modification of the vortex strength. It is not possible to accurately locate the core from the results, using for example the half width technique (Greenwell[7]) since the attached flow contribution is substantial. Near the hinge line, the elevon appears to cause a large effect on the attached flow as well as on the vortex.

As α increases, the elevon effect on the upper surface reduces. Movement of the burst point at α=15° can be seen from the clustering of the contours at x=250mm. As the burst point moves over a tapping in response to a change in η, there is a sudden change in C_p, particularly near the suction peak and this produces the pattern seen on fig. 12(b). The elevon does not produce as large an incremental loading on the burst portion of the vortex as for the unburst vortex, e.g. compare results at x=400mm for α=10° and 15°.

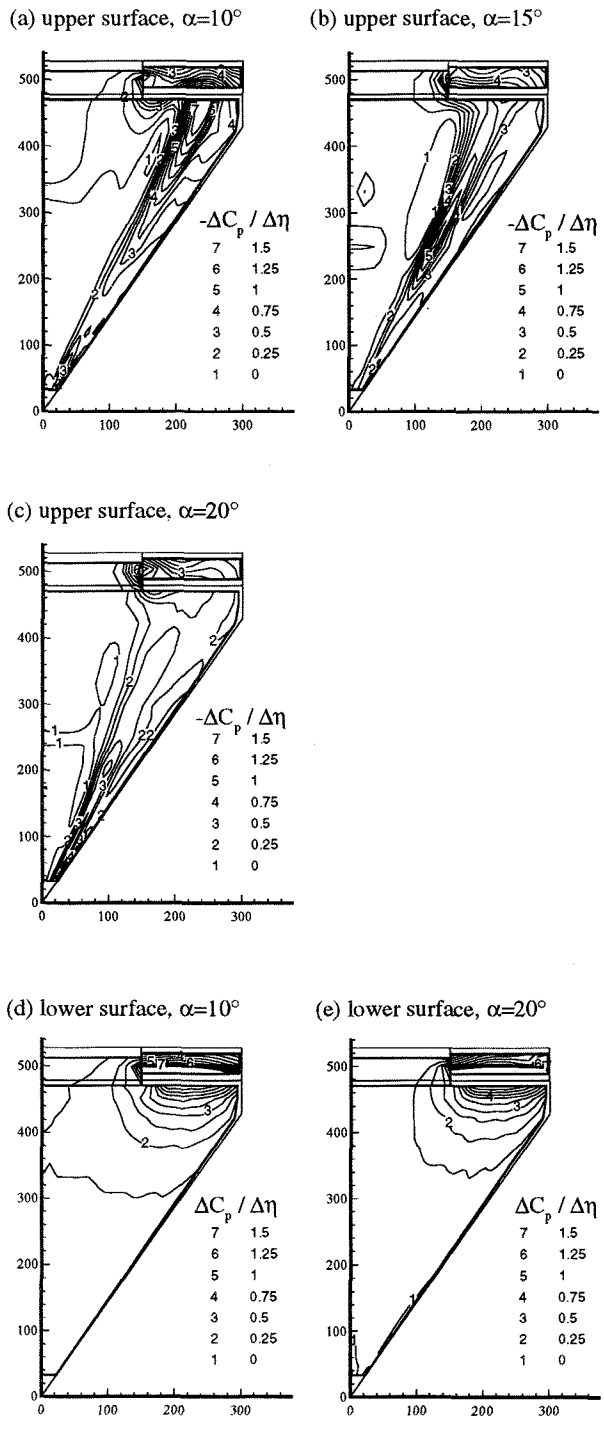

Fig. 12 - *incremental pressures for steady elevon deflections*

For the lower surface, the effect of $\Delta\eta$ is localised near the hinge line and elevon and the incremental pressures are constant with α.

Spanwise integration of the incremental pressures to give the incremental longitudinal loadings, further demonstrates these points (fig. 13). The lower surface loading is constant with α, whilst the upper surface reduces under the burst portion of the vortex, but is constant with α for the unburst portion. Again, the change in burst point location with η is illustrated by points 1 (α=15°) and 2 (α=12.5°) on the figure.

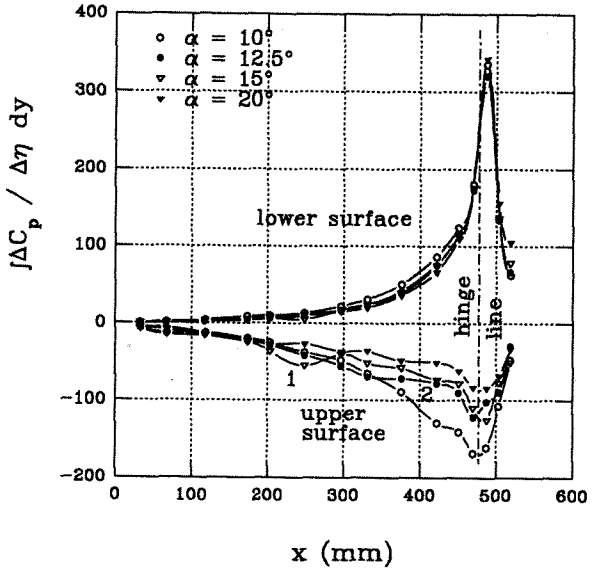

Fig. 13 - *spanwise integration of incremental pressures.*

UNSTEADY PRESSURE RESULTS

In order to determine the effects of the elevon oscillation on the wing bending mode and the elevon itself, it is necessary to consider the variation of the resulting unsteady pressures over the range of α and ν tested. Any variations with these two parameters would influence the need for scheduling of the terms within the matrix in fig. 1. The following section discusses the upper and lower surfaces separately though interaction between them does occur.

Fig. 14 shows the amplitude (C_{po}/η_o) and phase, ϕ, between the unsteady pressures and elevon motion, at α=10°, for ν=0.32, 0.98 and 1.65. By plotting -(C_{po}/η_o), the phase angles become easier to interpret, with ϕ=0° being in phase and positive ϕ being a phase lead. The amplitude of vortex strength oscillation is greatest under the vortex peak and lags the elevon motion (ϕ is negative). The phase lag under the main vortex suction is nearly constant with ν. It is important to remember that the instantaneous effective angle of the elevon, η_{aero} is dependent on both η and $\dot{\eta}$, since the angular velocity of the elevon produces an aerodynamic angle, i.e. assuming small angles,

$$\eta_{aero}(t) = \eta(t) + \frac{(x - x_h)\,\dot{\eta}(t)}{V}$$

This causes the effective shape of the elevon to be curved and the phase lead of η_{aero} compared with $\eta(t)$ to increase as ν increases. For example, when ν=1.65, η_{aero} leads $\eta(t)$ by 15°. Hence, the vortex lag relative to η_{aero} is actually increasing with ν although appearing constant with $\eta(t)$.

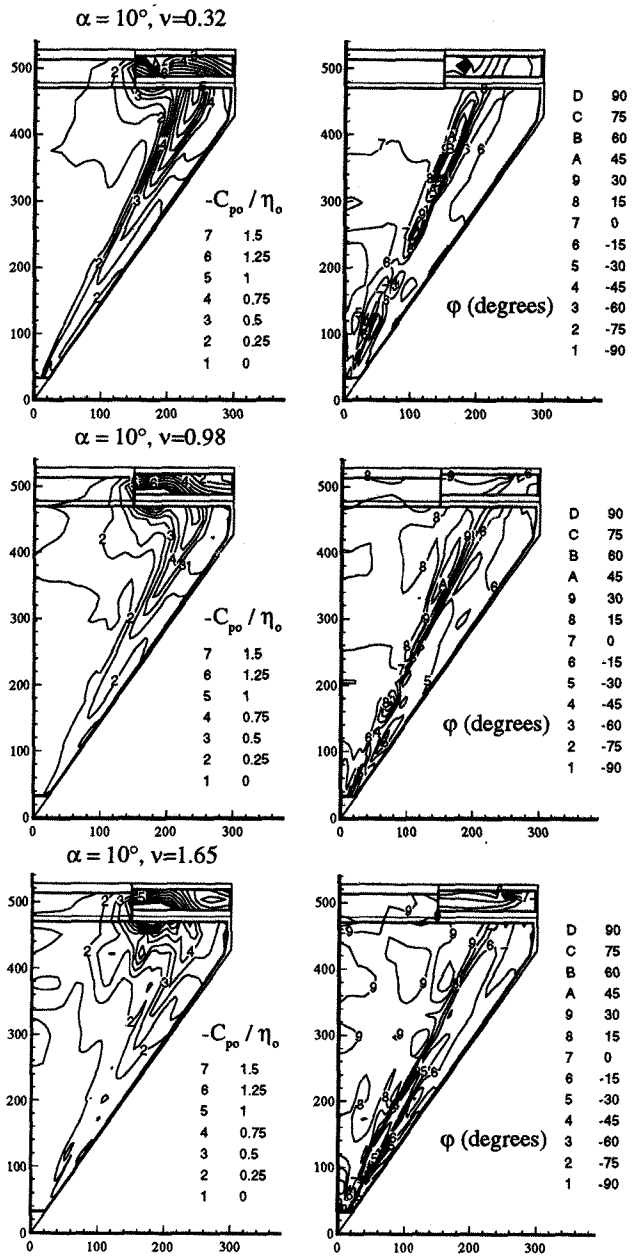

Fig. 14 - *upper surface unsteady pressures, α=10°.*

At ν=0.32, the unsteady pressure contours are similar to the steady incremental values of fig. 12(a), i.e. the gain is 1 (gain being the ratio between the unsteady amplitude at ν and that at ν=0). The gain towards the apex of the wing falls rapidly as ν increases, i.e. the vortex response to rapid elevon motion is reduced.

In fig. 14, at ν=0.32, there is a region centred at x=380mm, y=160mm, which extends towards the apex, where the pressures lead the elevon by a significant amount. This zone lies along the primary attachment line of the shear layer from the leading edge separation forming the vortex, and is due either to a delay in the effect of the elevon motion on the lower surface shear layer being transferred round to the surface or from the alteration in the vortex position and strength above the wing. Reconstruction of the total pressure levels (by adding the mean to the unsteady component at the elevon frequency) suggests there is a very slight lateral motion of the vortex which lags the elevon motion. The region of phase lead is also present to a lesser extent at the other frequency parameters shown.

At α=15°, ν=0.32 (see fig. 15), the dynamic burst point motion can be observed from the amplitude contours at x=300mm, and there is again a region of phase lead at the primary reattachment point near the burst location. Compared to the steady incremental loadings from fig. 12(b), the motion of the burst point is reduced in the oscillatory case (gain less than 1 in this area) and the gain for the unburst portion of the vortex is consequently much lower than one. The gain reduces rapidly with increasing α. The phase under the vortex core is constant with ν, as was the case at α=10°. The region of phase lead tends to consolidate at the primary attachment near the burst point of the vortex. These trends are also present at higher α.

Summarising the vortex response, as the burst point moves towards the apex the amplitude of the unsteady pressures, associated with the vortex suction peak, reduces rapidly (i.e. with increasing α). The lags compared to η_{aero} is not dependent on the burst position.

Returning to fig. 14, at α=10, the gain for the region near the hinge line and on the elevon remains near one throughout the range of ν tested. At α=15 (fig. 15), the unsteady amplitude on the elevon are also not affected greatly by the reduced frequency, ν within the range considered, although the amplitude levels are lower than at α=10°. The phase angles are similar for both angles-of-attack and increase with ν. The unsteady pressures on the elevon do not follow the trends of the vortex response. This suggests the elevon motion is having a significant effect on the attached flow in this area, rather than on the vortex itself.

Fig. 16 gives the lower surface unsteady pressures for ν=0.32 and 1.65. The amplitude is plotted as $+(C_{po}/\eta_o)$ since a positive deflection causes a positive increment in C_p. The effect of elevon oscillation is concentrated around the hinge line. At ν=0.32, the pressures are in phase with the elevon and the amplitudes are similar to those for steady elevon deflections (fig. 12(d)). At ν=1.65, the amplitudes are very similar to those at ν=0.32, but the pressures now tend to lead η(t). These lower surface trends are repeated at other incidences.

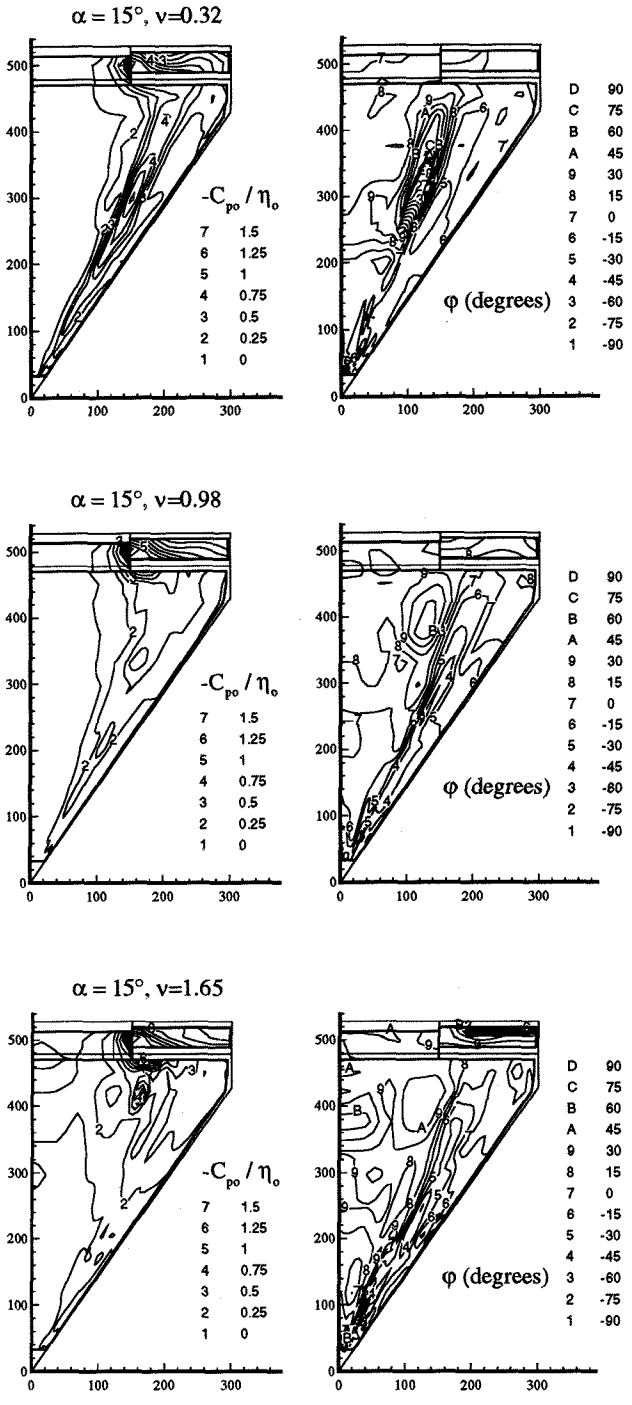

Fig. 15 - *unsteady upper surface pressures, α=15°*

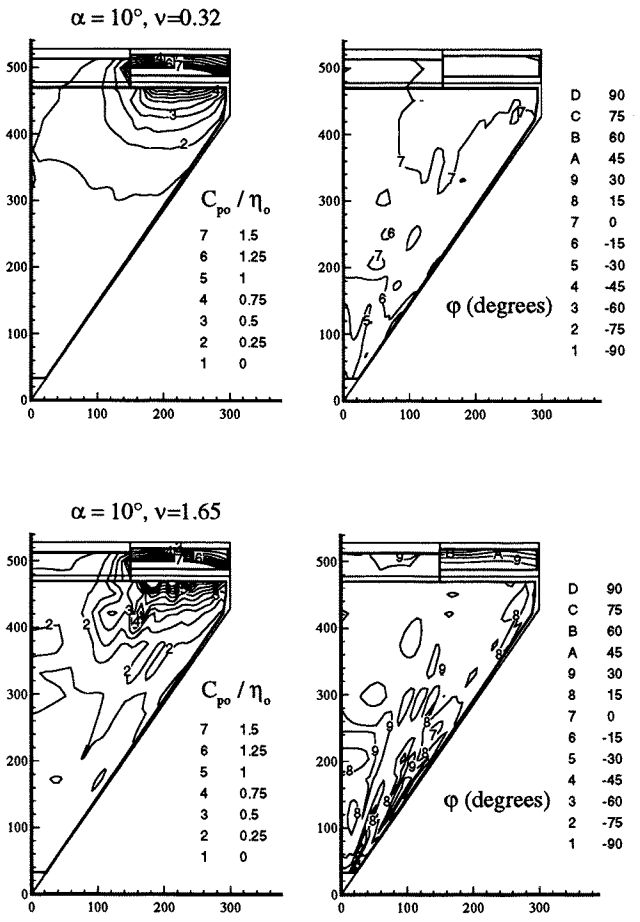

Fig. 16 - *lower surface unsteady pressures, α=10°.*

UNSTEADY HINGE MOMENTS

The unsteady hinge moments can be used as a measure of the diagonal control term in the matrices of fig. 1, i.e. the effect of elevon rotation on the elevon loads, Y. The values, from integration of the unsteady pressure results, incorporate the trends discussed in the previous section. By performing this integration to give an overall term, it is possible to determine the relative importance of the characteristics of individual regions and pressures with α and ν. Although the hinge moment is only produced by the pressures over the elevon, these are influenced by the interaction with the rest of the wing. The hinge moments are broken down into contributions from the upper and lower surfaces.

Fig. 17 shows the hinge moments, in terms of amplitude, h_o, and phase, ϕ_h, in relation to the elevon motion. The steady (ν=0) incremental hinge moments are shown for comparison. The lower surface contribution to hinge moment is double that of the upper surface and increases with α. The $h_{o,l}$ values tend towards the steady values. The phase, $\phi_{h,l}$, increases linearly with ν and is similar for all α.

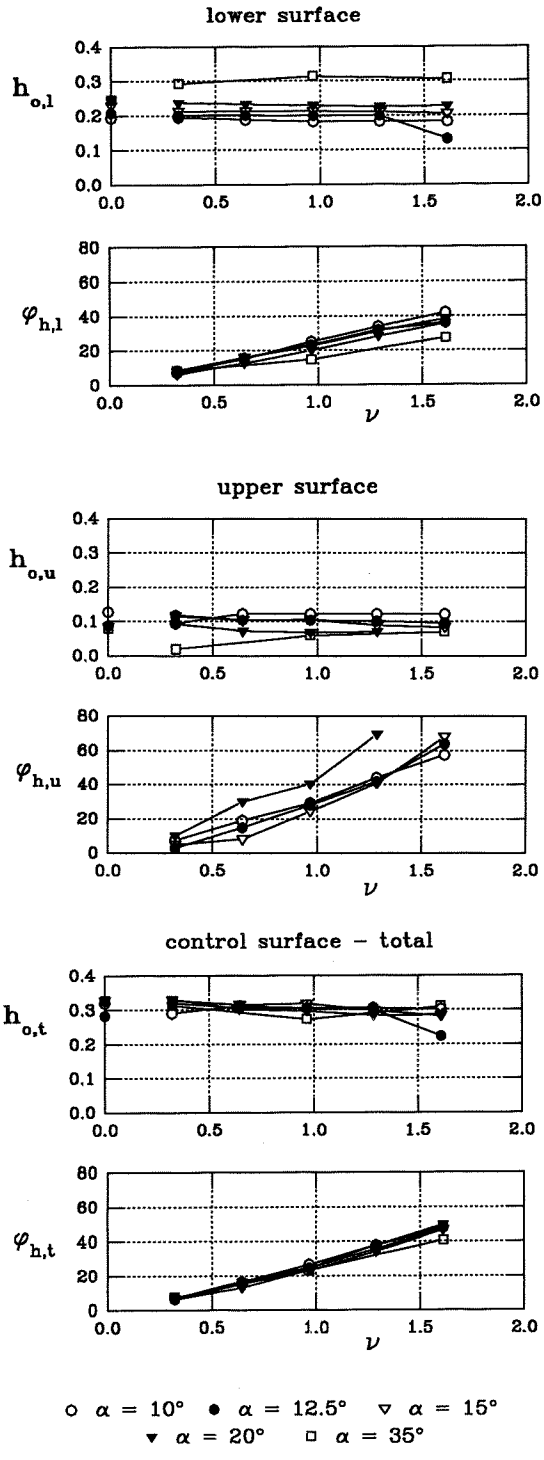

Fig. 17 - *unsteady hinge moments.*

For the upper surface, $h_{o,u}$ reduces with α, but is reasonably constant with ν and again correlates with the steady values. The $\phi_{h,u}$ are greater than $\phi_{h,l}$ though the trends are otherwise similar.

Combining the two surface effects, $h_{o,t}$ is constant with α and ν whilst phase increases with ν but is independent of incidence. This is largely due to the dominant effect of the lower surface. The increase in $h_{o,l}$ with α counteracts the reduction in $h_{o,u}$. These trends in unsteady hinge moment would require little scheduling in an FCS system (for the range of α and ν considered) and could be easily represented in the matrices. The steady results also give a good indication of the unsteady amplitudes.

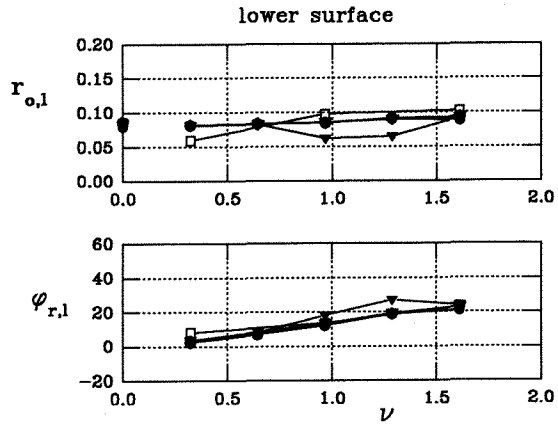

UNSTEADY ROOT BENDING MOMENTS

The unsteady root bending moments give an indication of the effect on a wing bending mode due to elevon rotation. Since the root bending at a point depends on the 'y' location, the regions near the tip and elevon have a large effect on the results, whilst those towards the apex where both y and (C_{po}/η_o) reduce are of less importance.

The root bending moment results are again split into the upper and lower contributions. The characteristics of these results are very similar to the hinge moments. The lower surface amplitude and phase (fig. 18) are independent of α up to α=20°, $r_{o,l}$ being constant with ν whilst $\phi_{r,l}$ increases with ν. For the upper surface, $r_{o,u}$ reduces with incidence whereas $\phi_{r,u}$ does not alter greatly with α except at α=35° where the vortex has broken down completely leaving a bluff body type flow. Unlike the hinge moments, the upper surface phase is less than that of the lower surface, since the response of the vortex tends to lag the elevon angle. This is partly countered by the large phase lead on the elevon itself.

Both the upper and lower results tend toward the steady incremental bending moment effects at low frequency parameters.

These surface contributions combine to give a total root bending moment of constant amplitude with ν, but which reduces with α (except at α=35° where the leeside flow has changed significantly). The phase increases with frequency parameter. The phase is lower than for the total hinge moments since the pressures in front of the elevon, which now contribute to the term, have an increasing phase lag relative to the pressures on the elevon.

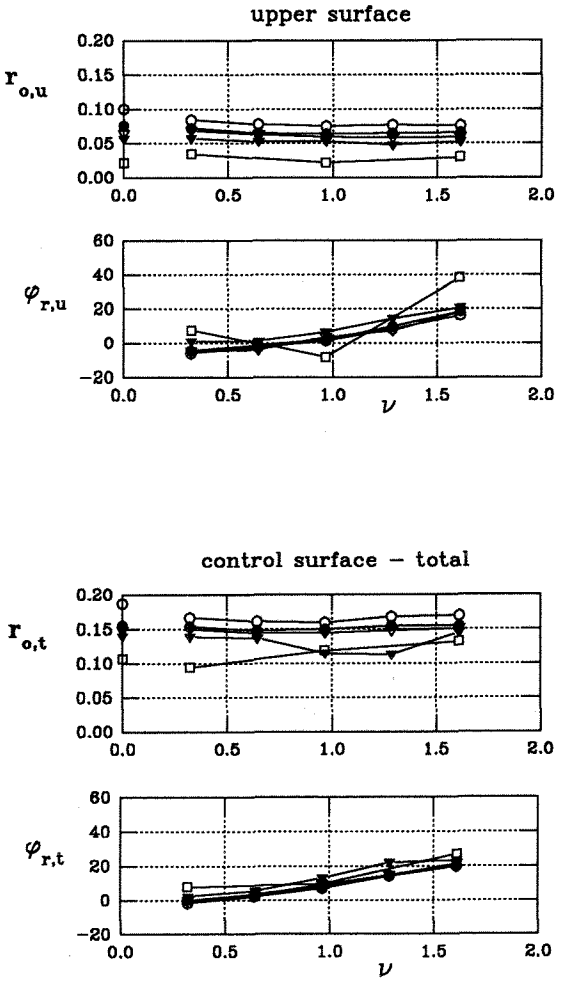

Fig. 18 - *unsteady root bending moments.*

CONCLUSIONS

For a 55° leading edge sweep wing, there is a relatively weak vortex present over the upper surface which bursts in front of the trailing edge for $\alpha\rangle 10°$.

The gain of the vortex response to elevon oscillation (ratio of amplitude of unsteady pressure component to steady incremental results) reduces rapidly with frequency parameter for both a burst and unburst vortex. The phase lag also increases with ν when compared to the actual instantaneous aerodynamic elevon angle, which leads the structural angle.

The unsteady amplitude of the attached flow on the lower surface is independent of both α and ν, whilst the phase lead increases with ν.

These effects combine to produce constant amplitude unsteady hinge moments (a measure of elevon effect on itself) with an increasing phase angle with ν. The unsteady root bending moment reduces with incidence and the phase angle increases with ν, but at a rate lower than the corresponding hinge moment results. The vortex response affects the trends in the root bending moment results, but less so the hinge moment results which appear to be produced by the effect of the mode on the attached flow for both the upper and lower surfaces. The amplitudes of both the hinge moments and root bending moments agree with the steady incremental moments.

These results give an indication of the likely effect of the elevon rotation mode on any rigid roll or bending modes. However, they only give an indication of the structural excitation. The actual structural response depends on the aerodynamic effect of the wing bending mode and the resulting interaction between the two modes, i.e. the other terms in the matrices of fig. 1.

REFERENCES

1. Ross, A.J., Control Derivatives, Paper 14 from AGARD CP 386.

2. Orlik-Rückemann, K.J., Unsteady Aerodynamics and Dynamic Stability at High Angles of Attack, lecture 8 from AGARD LS 121.

3. Lang, J.D. and Francis, M.S., Unsteady Aerodynamics and Dynamic Aircraft Manoeuvrability, Paper 29 from AGARD CP 386.

4. Williams, W.G. and Lockenour, J.L., Stability and Control Status for Current Fighters, Chapter 5 from AGARD AR 82.

5. Bergh, H., Tijdeman, H., Theoretical and Experimental Results for the Dynamic Response of Pressure Measuring Systems, N.L.R. Report No. F238, 1965.

6. Bergh, H. and Tijdeman, H., The Influence of Main Flow on the Transfer Function of Tube-Transducer Systems Used for Unsteady Pressure Measurements, N.L.R. Report No. mp 72023u, 1972.

7. Greenwell, D.I. and Wood, N.J., 'Determination of Vortex Burst Location on Delta Wings from Surface Pressure Measurements', AIAA Journal, Vol. 30, Nov. 1992.